Scaling of fault damage zones in carbonate rocks

Sylvain Mayolle, Roger Soliva, Yannick Caniven, Christopher Wibberley, Grégory Ballas, Gaétan Milesi, Stéphane Dominguez

1   # Scaling of fault damage zones in carbonate rocks

2

3   Sylvain Mayolle[a*], Roger Soliva[a], Yannick Caniven[a], Christopher Wibberley[b], Gregory

4   Ballas[a], Gaétan Milesi[a], Stephane Dominguez[a]

5

6   [a] Geosciences Montpellier, Université de Montpellier, Université des Antilles, CNRS, Rue

7   du Truel 34095 Montpellier, France

8   [b] TOTAL EP, CSTJF, Av. Larribau 64018 Pau, France

9

10   Corresponding author:

11   *sylvain.mayolle@umontpellier.fr, Geosciences Montpellier, Batiment 22, Rue du Truel

12   34095 Montpellier, France, (33) 4 67 14 38 94 (S. Mayolle)

13

14   Key words: *fault damage; displacement; carbonates; scaling law; segmentation*

15

16

17

Abstract

A renewed interest in fault damage zones is aimed at better understanding stress perturbation around faults, earthquake ground motions and fluid flow in the upper crust. In this study, we analyse fault/fracture systems at the outcrop and map scale and define *displacement - thickness* (*D-T*) scaling of fault damage zones using scanlines, in carbonate rocks in France and Spain. We determine fault displacement and damage zone thickness perpendicular to fault planes and far from fault tips for 12 selected faults in four study sites. The data show a logarithmic decrease of fracture frequency from the fault cores. This decrease is characterized by local frequency peaks corresponding to variably-linked secondary fault segments and abandoned tips within the fault damage zone. *D-T* data comprised between 0 and 100 m of net fault displacement show a nearly linear scaling with very little scattering. Including two additional data for *D* > 100 m, the best fit corresponds better to a power law. We propose a new model based on fault segmentation and linkage to explain the linear scaling observed up to 100 m displacement, and we discuss the non-linear behaviour with respect to the role of mechanical layer thickness and the inhibition of the segmentation process down dip for large-scale faults.

1. Introduction

Deformed rock volumes in fault zones are usually classified as two distinct zones, the Core Zone (CZ) and the Damage Zone (DZ) (Shipton and Cowie, 2001; Billi et al., 2003; Kim et al., 2004; Berg and Skar, 2005). The core zone is generally characterised by the presence of fault rocks (e.g. Sibson, 2000; Fossen, 2016) with variable comminution degree and frequently well-developed cementation, generally acting as a barrier of permeability when the

2

fault is dormant. The damage zone develops through different processes such as initiation, propagation/interaction of faults or seismic ruptures (Cowie and Shipton, 1998; Peacock, 2001; Shipton and Cowie, 2003; Kim et al., 2004; Peacock et al., 2017). Depending on the nature of the deformed rock and the applied state of stress, a wide diversity of damage structures can be found such as tensile fractures, layer folding, stylolites, dilation, shear and compaction bands. These structures may produce significant and variable impacts on permeability anisotropy in and adjacent to faults and therefore on fault-related fluid flow (Chester and Logan, 1986; McGrath and Davison, 1995; Caine et al., 1996; Sibson, 2000; Jourde et al., 2002; Kim et al., 2004; Agosta et al., 2007; Faulkner et al., 2010; Ballas et al., 2015). Despite their importance for economic fluids, fault damage zone 3D structure, their scaling and flow properties remain poorly known and still debated.

The geometry of damage zones has been described, from map, outcrop and microstructural analyses (McGrath and Davison, 1995; Billi et al., 2003; Micarelli et al., 2003; Johansen and Fossen, 2008; Choi et al., 2016). The *Damage zone thickness* (*T*) is defined as the total adjacent rock volume on both sides of the fault core containing brittle damage structures related to the fault (Shipton and Cowie, 2001, 2003; Berg and Skar, 2005; Schueller et al., 2013; Choi et al., 2016). Many studies indicate that *T* seems to evolve with the net fault *Displacement (D)* (e.g, Evans, 1990; Knott et al., 1996; Shipton and Cowie, 2003; Manighetti et al., 2004; Mitchell and Faulkner, 2009, 2012; Faulkner et al., 2011; Savage and Brodsky, 2011; Torabi and Berg, 2011; Perrin et al., 2016) and some of them even reveal a proportional relationship between *T* and *D* for *D* < 150 m (Shipton and Cowie, 2003; Mitchell and Faulkner, 2009, 2012; Savage and Brodsky, 2011; Schueller et al., 2013). For *D* > 150 m, *T* seems to stabilize at a few hundred metres. However, despite this evidence for a *D-T* relationship and associated trends, the processes and mechanics causing this remain difficult to constrain because of the large scattering of data used, about two orders magnitude (Savage

67 and Brodsky, 2011). Many factors can be responsible for this scattering. Firstly, the

68 methodologies used to measure or quantify T vary between studies with no systematic

69 consensus. By combining many different published studies into a large scanline database,

70 damage can be described by undifferentiated structures such as tensile fractures and

71 deformation bands, whose frequency decreases with distance from the CZ (e.g. Chester and

72 Logan, 1986; Beach et al., 1999; Schueller et al., 2013). Then, the external limit of the

73 damage zone is defined as the point where the fracture frequency reaches the background

74 fracture frequency value (Beach et al., 1999; Berg and Skar, 2005; Faulkner et al., 2006; de

75 Joussineau et al., 2007; Mitchell and Faulkner, 2009) although background fracture frequency

76 is usually difficult to determine, adding errors in the assessment of T. Secondly, the fault

77 damage types (tip damage, wall damage, link damage) in the sense of Kim et al. (2004) or in

78 the synthesis from Mitchell and Faulkner (2009) (also see Wilson et al., 2003; Blenkinsop,

79 2008), are not differentiated, probably also explaining a part of the D-T data scattering.

80 Thirdly, differences in rock type could also produce a strong effect on fault zone architecture

81 and potentially on the D-T scaling (e.g. Soliva et al., 2006; Roche et al., 2012; Ballas et al.,

82 2014). Most of the studies whose aim is to characterize the D-T scaling law are mainly based

83 on faults in siliciclastic lithologies (e.g. Knott et al., 1996; Fossen and Hesthammer, 2000; Du

84 Bernard et al., 2002; Berg and Skar, 2005; de Joussineau and Aydin, 2007; Mitchell and

85 Faulkner, 2009). Although carbonate fractured reservoirs are common and the understanding

86 of fracture network complexity represents a major issue for exploration/production of

87 georesources, the fault damage zones and their scaling properties are poorly constrained for

88 this lithology (Micarelli et al., 2003; Micarelli et al., 2006; Balsamo et al., 2016; Maqbool et

89 al., 2016).

90

91 In this paper, we focus on the analysis of fault damage in carbonate rocks. We first provide

92 a map scale analysis of fault segmentation geometry and damage using analysis based on

93 remote sensing orthophotos and outcrops. Secondly, we analyse small-scale fracture damage

94 using scanlines adjacent to fault, cores far from fault tip zones, and on outcrops where

95 displacement can be measured. This enabled the identification of 12 faults, on which we

96 define the *D-T* relationship. We analyse the resulting scaling laws and discuss their properties

97 with respect to the map scale observations and previous models proposed in the literature.

98 Finally, we propose new explanations based on fault growth processes, and especially fault

99 segmentation and linkage.

100

101

102 2. Geological setting

103 In this study, we focus on two areas located in the south of France (Languedoc) and close

104 to the Eastern coast of Spain (Sant Mateu and Maestrat). These two sites show normal faults

105 due to the Oligocene Mediterranean Sea opening and some reverse and strike-slip faults from

106 the Paleogene Pyrenean orogeny contraction, all in Tethysian mudstone carbonates.

107

108 2.1 *Languedoc (south of France)*

109 The Languedoc region is located in the former western gulf of the Tethys Ocean (Fig. 1a).

110 Most of the outcrops in the region contain marine sediments comprising stratified carbonate

111 rocks (Fig. 1a). The Mesozoic sedimentary cover can reach a total thickness up to 3,000 m. In

112 this study, the analysed faults only affect Jurassic and Cretaceous rocks. The Jurassic section

113 is characterized by sublithographic marine limestones and is several hundred metres thick.

114 The Cretaceous rocks are characterized by marl and massive limestone alternations with
115 ammonites and brachiopods fossils.

116 The Mesozoic cover was affected by Pyrenean shortening, expressed by three phases of
117 deformation from Paleocene to Oligocene (Petit and Mattauer, 1995; Séranne et al., 1995;
118 Benedicto et al., 1999). The first one is characterized by well-marked N020E-oriented
119 fractures (Taha, 1986; Arthaud and Laurent, 1995), and kinematically consistent thrust faults.
120 A second N145E oriented contraction is marked by N055E stylolites and N145E joints. A last
121 N-S contractional stage is visible with N-S joints and E-W stylolites. This last contraction
122 allows activation of the N020E joints and N055E stylolites in sinistral strike-slip (Petit et al.,
123 1999; Soliva et al., 2010). These faults have also been reactivated during the Oligocene
124 extension phase as normal faults (e.g. Arthaud and Mattauer, 1969).

125 Depending on the different accessibilities and outcrop quality in Languedoc area, this
126 study focuses on the St Clement normal fault, the Taurac reverse fault and two other minor
127 faults in the St Clement area. Like the crustal-scale Cevennes and Nimes faults, the St
128 Clement fault was probably active during 3 tectonic phases. (1) NW-SE middle Cretaceous
129 extension showing a normal phase of slip; (2) during the Paleocene to Eocene Pyrenean
130 shortening, a sinistral strike-slip phase; and (3) a main phase during Oligocene NW-SE Gulf
131 Lion rifting with around 550 m displacement on the fault (Arthaud and Mattauer, 1969; Steer
132 et al., 2011). The brittles structures are mainly consistent with normal faulting, but a minority
133 can be related to strike-slip events (Auzende et al., 1973; Séranne et al., 1995; Benedicto et
134 al., 1999; Steer et al., 2011). The Taurac fault is a reverse strike-slip fault connected to the
135 Cevennes fault. Striations on the main fault slip surface show reverse strike-slip and dip-slip
136 reverse displacement.

137

2.2 *Maestrat*

The second study area is located at the eastern border of the Maestrat basin (Fig. 1b). The Maestrat is a part of the Iberian Range, which contains several kilometres of Mesozoic and Cenozoic sediments (Nebot Miralles and Guimerà i Rosso, 2016). This region was affected by two phases of extensional rifting with NW-SE trending normal faulting, from the Triassic to the mid-Cretaceous (Albian), during which time were deposited the Jurassic shallow carbonate platform, Cretaceous carbonates and different layers of marls (Salas and Casas, 1993; Salas et al., 2001, 2011; Martín-Martín et al., 2013). During the Middle Eocene to Early Miocene, the Alpine orogeny affected the basin with a contractional deformation (González, 1989).

A general tectonic extensional event followed the Alpine inversion, and caused the Catalan and Valencian coastal rifts. During Late Oligocene to Early Miocene this extensional stage generated multiple NE-SE minor normal faults through the Mesozoic carbonates (Roca and Guimerà, 1992; Salas and Casas, 1993; Salas et al., 2001). In the Sant Mateu area (Fig. 1b), the Mesozoic rocks are tilted 30° to the NE and the lithologies are consistent with Languedoc carbonates. In the Aliaga area the N-S Alpine inversion, during late Oligocene and early Miocene, generate strike slip fault and reverse faults with south and north vergence (Fig. 1b). Mesozoic cover rises to over 1,000 m altitude, being tilted and folded (Nebot Miralles and Guimerà i Rosso, 2016). In this area, there is no evidence of Neogene extensional reactivation.

In summary, the Languedoc and Maestrat study areas show carbonate rocks that were deposited during the Tethys ocean opening and were deformed both during the Alpine contractional events, and the extensional rifting during the Late Oligocene to Early Miocene. In the Sant Mateu and St Clement areas, folding is gentle and there is no evidence of thrust faults in the vicinity of the area.

163

164

3. Methods

3.1 *Terminology of brittle damage structures*

In this study, discontinuous deformation of the carbonate rocks observed in the field are qualified by 4 different terms, joints, veins, stylolites, and faults, and are identified in the field depending on their geometric and kinematic properties (Fig. 2). The term joint refers to a Mode I fracture, from metric to decametric length, for millimetre to centimetre opening, not sealed or filled with druse calcite. Veins are defined as centimetric to metric Mode I fractures and always cemented with sparitic calcite. They can also be described as "tension gashes". Veins and joints are generally oriented perpendicular to the minor-principal stress axis (Fossen, 2016). A generic usage of the term "fracture" refers to both joints and veins. Veins and joints that affect carbonates are frequently preferential surfaces for dissolution, depending on cementation. In this study, three scanlines were made to sample structures on an outcrop that has suffered significant dissolution. In these cases dissolution patterns on the rock surface have been counted as fractures. Stylolites are dissolution surfaces also known as solution seams or Mode –I structures in carbonate rocks (Toussaint et al., 2018). They are perpendicular to the major-principal stress axis and also to veins or a set of joints.

Faults are slip planes of mode II or III tips of metric to kilometric length, generally showing one or multiple slickensides with slickenlines. DZ can include secondary minor faults and slickensides with a certain width of fault rocks in their individual CZs. Secondary faults in DZs are always indicated on the scanline histograms.

185

3.2 *Scanline measurements*

Measurement of fracture damage was performed along scanlines across the damage zones. A scanline consists of the fracture frequency measurement per linear metre along a sampling line. This frequency is also referred to as the fracture density (P10) as the number of fracture intersections along a 1D scanline (Dershowitz, 1984; Bisdom et al., 2014). The sampling step (Ws), the distance over which the number of fractures is counted, is adapted to the total scanline length (Ls). For Ls < 5 m, Ws = 10 cm; for $5 \leq L$s ≤ 20 m, Ws = 50 cm; for Ls > 20 m, Ws = 1 m. When Ws < 1 m, the frequency is normalized to be comparable with others dataset.

The scanline is oriented nearly perpendicular to the fault trace and starting at the boundary between the main CZ and the DZ. Moreover all the scanlines satisfy several other criteria including (1) the position of the outcrop far from the observed fault tips at the map scale (2) the outcrop must be large enough to reach the background fracturing, (3) the lithology must be similar through the entire scanline, and (4) the fault net displacement must be measurable. We selected 12 fault outcrops meeting all these criteria allowing measurement of fracture frequency along 12 scanlines noted S1 to S12. Two of these scanlines (S5 and S6) actually come from the same fault but were measured at different places and along different carbonate layers.

The fractures counted on the outcrops were those visible to the naked eye along scanlines, and several effects can generate "gaps" in the outcrop. The vegetation and outcrop degradation are the major sources of gaps. For the reverse Taurac fault, the scanline is positioned along the wall of an artificial tunnel and exposed to calcite precipitation and speleothems. These gaps are reported in the histograms of the scanlines as shaded areas, which represent a proportion of the scanline length ranging between 0% for the smallest faults (S1, S3, S7 and S10) up to 48% for the largest scanline (S2).

211   On the studied outcrops, dissolved fractures were counted separately from the sealed veins

212   on the histograms. The number of dissolved fractures thus brings together different types of

213   fractures, veins, joints, and sub-vertical stylolitic surfaces.

214

215   3.3 *Damage zone thickness*

216   The DZ thickness is estimated using the cumulative frequency curve (Berg and Skar, 2005;

217   Choi et al., 2016). The gaps in frequency value are corrected by adding an average value of

218   the two measurements before and after the gap. According to Berg and Skar (2005) and Choi

219   et al. (2016), the DZ thickness is defined by the distance to the fault core corresponding to the

220   inflection of the cumulative frequency curve. This inflection shows a stabilization of fracture

221   density away from the fault defined as the background fracturing. Most of the scanlines have

222   two inflections of the cumulative frequency curve. In this study, it is the farthest inflection

223   from the fault that is retained as the DZ thickness. This inflection corresponds to the value

224   where the cumulative frequency curve reaches the lowest slope gradient, which means a lower

225   and homogenous fracture density. The distance between the first and the second inflection is

226   considered as the half of the DZ thickness uncertainty.

227   The cumulative frequency curve used to define DZ thickness has several advantages (Choi

228   et al., 2016), including (1) a better detection of outer boundaries of the DZ based on the

229   intersection point of the cumulative frequency trends, (2) less influence of structural effects

230   like secondary faults on the general decay, and (3) a correction of the gaps based on adjacent

231   cumulative frequency gradient.

232   The apparent thickness defined along the scanlines is corrected as the real damage zone

233   thickness (*T*) using the angle between the scanlines and fault dip (Fig. 3). For the scanlines

234   acquired only on the footwall or the hangingwall, the DZ thickness value is doubled, as

235   proposed by Savage and Brodsky (2011). This value is very close to the "Total fault zone

236 thickness" used in literature, which actually includes the CZ thickness. The core zone

237 thickness could not be measured for all the faults, but its thickness generally correspond to

238 values lower than one order of magnitude of the DZ thickness (e.g. Childs et al., 2009;

239 Fossen, 2016), and is therefore smaller than the estimated error.

240

241 3.4 *Fault displacement*

242   The scanlines are always acquired on faults whose displacement is quantifiable.

243 Displacement (or net slip, *D*, Fig. 3) is determined using both fault surface dip, slickenline

244 orientation, layer dip and the offset between fault cutoff lines. In cases where slickenlines or

245 fault surfaces were not observed in the field (4 faults, referred to S7, S9, S10 and S11), we

246 used the average of fault dip and slickenline data measured in the considered studied fault

247 system. To define the error bars, we consider a minimum and maximum value of

248 displacement using +/- 30° for the pitch of the value measured on the outcrop, or the mean

249 value used for faults without slickenlines.

250

251 3.5 *Fracture orientations*

252   On all the scanlines, fracture orientations were systematically recorded along the profile to

253 characterize the fault damage fracture trends with respect to background fracturing. These

254 measurements have been made to identify the orientation of each type of deformation

255 structure exposed in Section 3.1, and to verify that fracture orientations are sub-parallel and

256 consistent with the orientation of the main fault. Field measurements were conducted using

257 mini-tablets and FieldMove Clino ©Copyright Midland Valley Exploration Ltd 2014. The

258 data were regularly double-checked with a classical compass and clinometer to check the

259 potential deviation of the mini-tablet measurements (Allmendinger et al., 2017; Novakova and

260 Pavlis, 2017). The treatment of fault and fracture plane orientations and their representation

261   on a stereogram has been done with the software Stereonet, R. W. Allmendinger © 2006-

262   2016. Because of the large amount of fracture data, and their planes often being vertical, we

263   represent them as "rose diagrams". The orientations have also been measured for the

264   background fracturing between faults, along outcrops distributed between faults at map scale.

265

266   3.6 *Map scale analysis*

267   Brittle damage at the map scale was characterized from geological maps, orthophotos of

268   0.5 m pixel size (PNAO from Centro Nacional de Information Geografica, ORTHO HR®

269   from IGN), measured in the field, and synthetized into the QGIS 2.18 software for precise

270   interpretation of the structures in the study area (Fig. 4 and A1). The main brittle faults being

271   characterized by Earth surface objects (reliefs, shadows, layer and rock discontinuities, limits

272   and lineaments in the vegetal cover), fault mapping is mainly derived from orthophoto

273   lineaments (Clark and Wilson, 1994). A manual lineament interpretation approach allowed

274   geological and anthropic lineaments to be distinguished. In many cases, vegetation,

275   Quaternary sediments and anthropic cover provide significant censoring biases for more than

276   50% of the studied areas. This particularly affects the detection of small lineaments lower

277   than 100 m in length, such as small faults and all Mode I fractures, that cannot be detected

278   with such a method. To characterize Mode I and stylolite background fracturing at this map

279   scale, we measured their orientation and density along 47 outcropping stations between faults.

280

281

4. Damage Zone analysis

4.1 *Map scale analysis*

The St Clement and Sant Mateu study areas allow the map-scale analysis of master fault geometry and the spatial distribution of secondary faults only (Fig. 4 and A1). The master fault observed on the West side of the Sant Mateu area is shown in Fig.4a. This master fault is formed of fault segments, with variable degrees of interaction (open relays, e.g. at Salzadella, Fig. 4b, or linked relays). The uplifted eastern side of this master fault exhibits many unlinked, adjacent secondary-fault segments. These secondary fault segments define a zone of brittle faulting adjacent to the master fault, which increases towards the northern fault tip. This type of secondary fault tip damage pattern at a smaller scale is also observed with small lineaments (Fig.4b). Note however that truncation and censoring biases are too large at this scale to correctly analyse fault damage patterns close to the secondary faults. In the St Clement area, the master fault is also composed of more or less linked fault segments (Fig. A1). Secondary fault patterns are observed close to the master fault tips, but also at its centre around a linked relay composed of two master fault segments.

Outcrop data show Mode I fracture mainly trending N030E to N060E, which is consistent with the main lineament orientations, secondary faults and the master fault (Fig. 4c). In St Clement, both fracture and lineament orientations are more scattered, between N030E and N090E, and that fracture orientations are more perturbed in relay zones at both sites. Fracture densities counted in these outcrops between faults allows a characterization of background fracturing, giving a P10 density ranging between 15 and 17 Mode I fracture/m.

4.2 *Scanline analysis*

In this section, we present the data of 12 scanlines (S1 to S12, Fig. 5), taken from 11 different faults. A total of more than 14,800 fractures were counted on all the scanlines. The

307   S1, S2, S3 and S4 scanlines (Fig. 5a, b, c and d) were acquired in the Languedoc region

308   (France); the S5, S6, S7, S8 and S9 (Fig. 5e, f, g, h and i) scanlines were acquired in the Sant

309   Mateu area (Spain) and S10, S11, S12 (Fig. 5j, k, l) were acquired in the Aliaga area (Spain).

310   Scanline S8 illustrates the decrease of damage decay with distance from a normal fault

311   oriented N097E 67°S, with a slickenline of 70°SW pitch (Fig. 6). Its displacement is

312   estimated at 27 m. The number of sealed fractures clearly shows a decrease along the profile

313   away from the main fault. As for scanline S8 (Fig. 5h and Fig. 6), all the scanlines show a

314   decrease in the frequency of sealed veins with increasing distance (Fig. 5). This decay can

315   have different shapes and can be distributed along the entire scanline, or localised close to the

316   main fault. The decay of fractures in S8 is not continuous, with a polymodal shape marked by

317   fracture frequency peaks present in both the inner and the outer damage zone. These peaks

318   systematically correspond to secondary faults observed at the outcrop. When the displacement

319   is greater than 50 m, the faults are often accompanied by minor faults in the damage zone of

320   the main fault (S2, S4, S6, S9, and S12 see Fig. 5b, d, f, g, and l). These minor faults have

321   small displacements, i.e. centimetric to metric. These secondary faults are always

322   accompanied by fractures frequency peaks, and can be the maximum of fracture density of the

323   entire scanline. Furthermore, when the displacement is lower than 50 m, several fractures

324   frequency peaks are present on the scanline. These peaks mark secondary fault initiation or tip

325   damage of another segment as in Fig. 2d. These secondary faults are observed at different

326   scales and dimensions, on scanlines (Fig. 5), in the field (Fig. 2d) or in map view (Fig. 4).

327   The stereograms representing fracture orientations by typology (Fig. 6c) show that the

328   veins and joints have on average the same orientation (N160E and N090E). In these

329   stereograms, as in each stereogram representing fractures without distinction of typology (Fig.

330   6), the most represented orientation is sub-parallel to the main fault, except close to the main

331   fault. The dip of these fractures is from 50 to 80° NW, also sub-parallel to the main fault.

332   On all the scanlines, stylolites do not show clear frequency decay, being of generally

333   constant frequency overall along the scanline (except on S1 and S3). Along the S8 profile,

334   two sets of stylolites are measured, (1) a sub-vertical set between 80° and 90° dip and nearly

335   perpendicular to the fractures, and (2) a nearly horizontal set dipping 20° to 30° to the East,

336   nearly parallel to the stratification. In the damage zones, we also observe fracture sets and

337   stylolites with trends inconsistent with the Oligocene extension, revealing that a small

338   proportion of the fractures, consistent with the absolute background fracture density, are

339   present into the damage zones.

340

341   ### 4.3 *D-T scaling law in carbonate rocks*

342   Fig. 7 shows *Damage zone thickness* and *Displacement* values estimated from the faults

343   shown as scanlines in Fig. 5. The data acquired in the studied carbonate rocks clearly show a

344   normal correlation between *T* and *D* on a log/log diagram (Fig. 7). They are continuous over

345   three orders of magnitude of displacement and show little dispersion (Fig. 7).

346   The data fit to a power law of the type function in the form of:

347
$$y = Cx^{\alpha}$$
348

349   *C* being a constant and α the exponent, which is a real between 0 and 1 (Fig. 7a). The least

350   square coefficient of the trend is $R^2 = 0.93$, in which α equals to 0.82, then very close to an

351   affine relation, and *C* equals 1.6.

352   The function shows a good fit with the data from faults where D < 100 m. The *D-T* data

353   follow a near-linear *D-T* law with a correlation coefficient of 0.97 (Fig. 7c and d). In contrast,

354   in this part of the graph, literatures data are scattered over more than two orders magnitude

355   (Fig. 8). Total damage zone thickness of St Clement (S4) and Taurac (S2) faults are clearly

356   under the linear *D-T* scaling law. As these faults have displacements of 556 m and 516 m

357 respectively, this finding is coherent with the literature data and the *D-T* scaling law for

358 displacements over 150 m.

359

360

5. Discussion

362   The determination of the displacement and the DZ thickness based on 12 scanlines reveals

363 a well-defined *D-T* scaling relationship, characterised by a nearly-linear scaling over three

364 orders of magnitude of displacement and for displacement below 100 m. Over the value of

365 100 m displacement, the only two faults that can be measured define a bend in the scaling

366 relationship suggesting that DZ thickness may saturate around 150 m.

367

5.1 *Scattering in the D-T scaling*

369   Damage zone scaling relationships for faults with displacement lower than 100 m shows a

370 least square coefficient of $R^2 = 0.97$ with an exponent $\alpha = 0.95$, i.e. very close to a linear

371 scaling relationship. The accuracy of this data set contrasts with the scattering observed in the

372 Savage & Brodsky (2011) data compilation from various studies Fig. 8. Compared to this data

373 compilation, the data presented in Fig. 7 were acquired exclusively in non-porous carbonate

374 rocks, far from the fault tips and with the same methodology to estimate the DZ thickness. In

375 particular, the fact that scanlines have been acquired far from the fault tips, probably

376 contributes to reducing the scattering (Kim et al., 2004, Perrin et al., 2016). This suggests that

377 the spread of data observed in Savage & Brodsky (2011) can be due to several geological

378 factors and processes, including the rheology of the host rocks and the fault zone (Berg and

379 Skar, 2005; Fossen and Rotevatn, 2016; Philit et al., 2018), modalities of slip accumulation

380 (incremental ruptures, characteristic rupture size, creep; Hadizadeh and Law, 1991; Robert et

381 al., 1995; Gratier et al., 1999), but also to the method of determination of the damage

382 thickness (Choi et al., 2016) and fault net slip.

383   In our approach, the method for determining fault displacement depends on both the offset

384 of the layer and slickenline orientations measured in the field. The main source of error

385 concerns the slip vector, and a quite large uncertainty has been considered in the error

386 calculation (see Section 3.5). However that error bar for the displacement values is still

387 generally lower than the error bars obtained for damage zone thicknesses (see Figs. 7 and 8).

388 Although the error bar is quite large on damage zone thickness, the D-T values are much less

389 scattered than the data provided by previous studies (Fig. 8). This is probably due to an

390 improved consistency in the criteria chosen to measure fault damage and (Section 3.2), and a

391 more restricted set of geological variables (e.g. same lithology).

392   Despite working in the same lithology and the same methodology, damage thickness

393 values include some errors and uncertainties related to outcrop quality and therefore damage

394 zone thickness determination. In some of the scanlines, outcrop comprises gaps due to

395 weathering and vegetal cover, potentially affecting the trend in frequency decay. The

396 determination of the damage zone thickness is less robust for large faults where the gaps can

397 represent, in the worst case, 48% of the scan-line. In our study, for large faults such as S2 and

398 S6, the DZ thickness might be underestimated due to the lack of outcrop continuity, or

399 especially for S4 and S2, due to the scanline size which appears insufficient in length. Faults

400 S4 and S2 are actually within the scale range of fault displacement at which the linearity of D-

401 T scaling is generally considered lost and critically discussed in terms of data scattering

402 (Savage and Brodsky, 2011; Mitchell and Faulkner, 2012) (Fig. 8). For these two faults, the

403 mean fracture density observed at the end of the scanline is around 20 and 23 fractures/m,

404 which close to the background fracture density measured far from the faults (15 fractures/m)

405   from the map scale fracture analysis (see section 4.1, Fig. A1). This suggests that the

406   scanlines for these two faults are actually large enough to reach the background fracturing.

407

408   ## 5.2   *Damage zone growth model*

409   ### *5.2.1   Segmentation and linear D-T scaling*

410   Several conceptual and numerical models have been proposed to account for the growth of

411   damage zones around faults, including processes of fault propagation, fault slip accumulation,

412   and subsequent fault and fracture coalescence (e.g. Shipton and Cowie, 2001; Manighetti et

413   al., 2004; Micarelli et al., 2006; Childs et al., 2009; Faulkner et al., 2011; Schueller et al.,

414   2013). With the exception of Shipton and Cowie (2003), these models fail to explain a normal

415   correlation between displacement and DZ thickness. The slip-patch model of Shipton and

416   Cowie (2003) relates fault damage growth to the quasi-static stress distributed around the

417   incremental ruptures (also possible for dynamic ruptures, Griffith et al., 2009), and to the way

418   the fault ruptures in different places during its growth history. Although very interesting, and

419   probably accounting for the damage zone growth of an isolated fault, this model does not

420   clearly account for the major and well-known process of fault growth by segment linkage

421   inherent to most, fault systems (e.g. Peacock and Sanderson, 1991; Mansfield and Cartwright,

422   1996; Cowie, 1998; Soliva and Benedicto, 2004).

423   Segment linkage appears to be a prominent process of fault growth within the development

424   of fault populations (e.g. Peacock, 2003, and references therein), including the fault systems

425   studied here, and the concept has also been used to explain the step-wise development of fault

426   core zones and overall fault zone thickness development in general (Wibberley et al., 2008;

427   Childs et al., 2009). It therefore has significant impact on fracture frequency decay around

428   fault and damage zone growth. In most of the scanlines Fig. 5, the logarithmic decay of

429   fracture frequency is actually formed through addition of smaller secondary peaks of fracture

430   frequency. These fracture clusters have modal values decreasing toward the outside edges of

431   the fault damage zone and are generally related to the presence of secondary faults. In other

432   words, fault damage zones are actually formed of secondary faults with their own damage,

433   and in this way the entire topic of the damage zone thickness definition is a multi-scale

434   phenomenon. Complementary observations of the fault architecture in the field (Fig. 2d) or at

435   the map scale (Fig. 4 and A1) show that these faults are always composed of multiple partially

436   or fully linked segments at different scales, for both out-of-plane and in-plane observations

437   (also see section 4.1). These faults, as many others in fault systems, are formed of linked

438   faults segments, with abandoned tips (e.g. Peacock and Sanderson, 1991) or aborted small

439   faults in the stress drop zone of the master through-going fault (e.g. Gupta and Scholz, 2000),

440   with their own small damage zones. Such geometries are commonly observed in fault systems

441   and are inherent to scale invariant 3D fault patterns having linear *Displacement – Length*

442   scaling and fractal fault size distribution (e.g. Scholz and Cowie, 1990; Dawers et al., 1993;

443   Cowie et al., 1995; Cladouhos and Marrett, 1996; Schlische et al., 1996; Cowie and Shipton,

444   1998).

445   Fault segment linkage has also been identified as a self-similar process in terms of fault

446   displacement and spacing at relay zones (Peacock, 2003; Soliva and Benedicto, 2004;

447   Acocella and Neri, 2005; Fig. 9b). On a broad range of scales (i.e. displacement ranging

448   between 10^{-3} m and 10^{3} m), two fault segments are generally linked for a value of

449   displacement close to the value of spacing between them (Soliva and Benedicto, 2004). This

450   process of linkage therefore allows both the accumulation of displacement and fault damage

451   thickness by incorporating (1) the secondary damages of the former segments, (2) abandoned

452   tips and (3) small faults (Fig. 9a and d). In other words, fault linkage allows the creation of a

453   master fault and incorporation of both types of damages, i.e. wall, tip and link damages of

454   former segments at its vicinity. If this process is scale invariant the thickness of fault damage

455   must increase proportionally with displacement as proposed in Fig. 9c.

456

457   *5.2.2   Non-linear D-T scaling*

458   Although debatable, the *D-T* data obtained on the two largest faults (Fig. 7 and 8) define a

459   trend consistent with those observed by Savage and Brodsky (2011) and Mitchell and

460   Faulkner (2012). In both of those studies, a *D-T* linear scaling is observed up to a scale of

461   displacement of 100 – 150 m whereas lower or no increase of DZ thickness is observed for

462   larger fault displacement (Fig. 8). This however contrasts with what Perrin et al. (2016) show

463   from map scale analysis of damage only formed of secondary faults, especially close to fault

464   tip, such as the "tip damage" in the terms of Kim et al. (2004), or "parent fault" in the terms of

465   Marchal et al. (1998). This might be because at a certain scale, fault damage defined by Mode

466   I fractures (or deformation bands) is limited and that fault damage might still be present in the

467   form of secondary faults, far enough from the master fault and therefore not considered in

468   scanline analyses. We tested this hypothesis by reporting a DZ thickness obtained from map

469   analysis of secondary faults around the main faults in the Sant Mateu and St Clément study

470   areas (see section 4.1, Fig. 4 and Fig. A1). We also added data from the Têt fault zone cutting

471   crystalline rocks in the Pyrenees (Taillefer et al., 2017), which was also examined using

472   scanline and map analysis. These new data obtained at this scale suggest that fault damage

473   due to Mode I fractures might scale very differently to fault damage derived from secondary

474   faults only. This might be particularly expressed close to the tip of master faults, where Mode

475   I fracture damage should decrease in thickness towards the tip of the master fault as

476   displacement decreases to zero, whereas tip damage observed for secondary faults increases

477   towards the master fault tip, and scales with fault length (Perrin et al., 2016; Fig. 9d and Fig.

478   10). The scanline method is however fully efficient to define and understand the scaling of

479 Mode I fracture damage and to plot together enough data. Mapping of Mode I fracture or

480 deformation band damage around faults is rarely possible (e.g. Flodin, 2003; Davatzes et al.,

481 2005; Shipton and Cowie, 2003) and generally biased.

482   Several solutions might be envisaged to explain a non-linear scaling of Mode I fracture

483 damage. The first one was proposed by Ampuero and Mao (2017), on the basis that fracture

484 damage mainly results from co-seismic events (Griffith, 2009 and Aben et al, 2016) and

485 which extent is limited by the thickness of the brittle crust hosting earthquakes. Fault ruptures

486 restricted to the brittle crust and related stress perturbations do not increase proportionally in

487 length and height (also see Soliva et al., 2006) and therefore imply scale-dependent rupture

488 and damage properties, or at least that the thickness of the brittle crust is an upper limit to

489 scale independence. An additional model proposed here is based on the segmentation model

490 exposed in Section 5.2.1. Faults with displacements larger than 100 m might have a lower

491 fault tip reaching the brittle-ductile transition (Schlische et al., 1996; Nicol et al. 1996;

492 Manighetti et al., 2001), and will not be able to link with new fault segments down dip (Fig.

493 10). This change in crustal rock behaviour prevents fault linkage, link damage processes and

494 the accumulation of fault damage from former faults segments. This process must also favour

495 normal and reverse fault weakening by asperity removal such as proposed by Childs et al.

496 (2009), and therefore inhibits asperity damage processes for such faults (e.g. Mitchell and

497 Faulkner, 2009). Other types of scale dependent behaviour were documented in fault system

498 scaling laws (size distribution, *Displacement – Length*) where faults are restricted at the base

499 of the crust or major layer discontinuities within the brittle crust, and where few or no faults

500 are able to cut the underlying units due to (1) its specific behaviour, or (2) a limited amount of

501 remote strain (Ackermann et al., 2001; Bohnenstiehl and Carbotte, 2001; Soliva and Schultz,

502 2008). In some cases, this process can happen at the scale of stratigraphic units (Soliva et al.,

503 2006), at which non-linear damage scaling has also been observed (Micarelli et al., 2006).

504   Finally, an additional model of scale dependent fault damage could be considered given

505   that a significant part of the fractures might form during the interseismic periods such as

506   described by Robert et al. (1995). Carbonate rocks in particular express pressure solution

507   processes, which generally form during these interseismic periods or during fault creep.

508   Although the scanlines of Fig. 5 are not correctly oriented to count stylolites, they generally

509   show their presence in the damage zones, with kinematically coherent orientations in relation

510   to Mode I fractures. Their specific localisation close to fault cores documented by Benedicto

511   and Schultz (2010) in carbonate rocks, suggests that a part of fault damage strain is due to

512   slow deformation, although the proportion remains unclear. It is worth noting that, for strike

513   slip fault, slow interseismic strain is distributed around faults following an arctangent

514   function, with wavelength being related to the fault locking depth and therefore the brittle-

515   ductile transition depth (Savage and Burford, 1973). This potentially provides an additional

516   process to explain non-linear scaling of fracture damage, especially for strike-slip faults

517   documented by Savage and Brodsky (2011) at large scale. Such a hypothesis currently suffers

518   from lack of field data on interseismic fracture damage and definitions of the fault locking

519   depth, if any. Other potential processes generating fault damage, such as Mode I fractures due

520   to fault-related folding, are also hard to demonstrate from these field data due to the lack of

521   layer dip variations in the examples studied.

522

523

524   **6. Conclusions**

525   We present new results about fault damage in carbonate rocks combining fault system

526   analysis at map scale and *D-T* scaling, implying the following main results:

527   1) The scanlines obtained from field data show a clear logarithmic decrease of

528   fracture frequency as distance increases from the main fault, with local frequency

529   peaks in the damage zone corresponding to secondary faults.

530   2) Faults are formed of linked segments and abandoned tips in the fault damage zones

531   thickness.

532   3) *D-T* data comprised between 0 and 100 m fault displacement show a nearly linear

533   *D-T* scaling (power law with exponent of 0.95, with a least square coefficient R^2 =

534   0.97).

535   4) Including two additional data with D > 100 m, the best fit is a power law with an

536   exponent of 0.82 and R^2 = 0.93. As suggested by previous studies on fault damage

537   zones, damage thickness tends to saturate with increasing displacement larger than

538   100 m, and such an upper bound may be related to mechanical unit thickness.

539   5) These new data are discussed with respect to fault segmentation observed in the

540   field. We propose a new model which explains *D-T* scaling by fault growth

541   through segment linkage and damage zone thickness accumulation.

542   6) *D-T* scaling data of the largest faults, as well as data from the literature for

543   different rock types, suggest that Mode I fracture damage might be scale dependent

544   for *D* > 100 m. This is discussed in terms of inhibition of the down-dip

545   segmentation process and asperity weakening for crustal scale faults able to cut the

546   entire brittle crust.

547

548

549

555

References

F.M. Aben, M.-L. Doan, T.M. Mitchell, R. Toussaint, T. Reuschl´e, M. Fondriest, J.-P. Gratier, and F. Renard. Dynamic fracturing by successive coseismic loadings leads to pulverization in active fault zones. Journal of Geophysical Research: Solid Earth , 121:1–23, 2016. doi: 10.1002/2015JB012542.

Ackermann, R.V., Schlische, R.W., Withjack, M.O., 2001. The geometric and statistical evolution of normal fault systems: an experimental study of the effects of mechanical layer thickness on scaling laws. Journal of Structural Geology 23, 1803–1819.

Acocella, V., Neri, M., 2005. Structural features of an active strike-slip fault on the sliding flank of Mt. Etna (Italy). Journal of Structural Geology 27, 343–355.

Agosta, F., Prasad, M., Aydin, A., 2007. Physical properties of carbonate fault rocks, fucino basin (Central Italy): implications for fault seal in platform carbonates. Geofluids 7, 19–32. https://doi.org/10.1111/j.1468-8123.2006.00158.x

Arthaud, F., Laurent, P., 1995. Contraintes, déformation et déplacement dans l avant-pays Nord-pyrénéen du Languedoc méditerranéen. Geodinamica Acta 8, 142–157.

Allmendinger, R.W., Siron, C.R., Scott, C.P., 2017. Structural data collection with mobile devices: Accuracy, redundancy, and best practices. Journal of Structural Geology 102, 98–112. https://doi.org/10.1016/j.jsg.2017.07.011

Ampuero, J.P., Mao, X., 2017. Upper Limit on Damage Zone Thickness Controlled by Seismogenic Depth. In: Thomas, M.Y., Mitchell, T.M., Bhat, H.S. (Eds.), Geophysical Monograph Series. John Wiley & Sons, Inc., Hoboken, NJ, USA, 243–253. https://doi.org/10.1002/9781119156895.ch13

Arthaud, F., Mattauer, M., 1969. Exemples de stylolites d'origine tectonique dans le Languedoc, leurs relations avec la tectonique cassante. Bulletin de La Société Géologique de France 7, 738–744.

Auzende, J.M., Bonnin, J., Olivet, J.L., 1973. The origin of the western Mediterranean basin. Journal of the Geological Society 129, 607–620. https://doi.org/10.1144/gsjgs.129.6.0607

Ballas, G., Fossen, H., Soliva, R., 2015. Factors controlling permeability of cataclastic deformation bands and faults in porous sandstone reservoirs. Journal of Structural Geology 76, 1–21. https://doi.org/10.1016/j.jsg.2015.03.013

Ballas, G., Soliva, R., Benedicto, A., Sizun, J.-P., 2014. Control of tectonic setting and large-scale faults on the basin-scale distribution of deformation bands in porous sandstone (Provence, France). Marine and Petroleum Geology 55, 142–159. https://doi.org/10.1016/j.marpetgeo.2013.12.020

Balsamo, F., Clemenzi, L., Storti, F., Mozafari, M., Solum, J., Swennen, R., Taberner, C., Tueckmantel, C., 2016. Anatomy and paleofluid evolution of laterally restricted extensional fault zones in the Jabal Qusaybah anticline, Salakh arch, Oman. Geological Society of America Bulletin 128, 957–972. https://doi.org/10.1130/B31317.1

Beach, A., Welbon, A.I., Brockbank, P.J., McCallum, J.E., 1999. Reservoir damage around faults; outcrop examples from the Suez Rift. Petroleum Geoscience 5, 109–116. https://doi.org/10.1144/petgeo.5.2.109

Benedicto, A., Séguret, M., Labaume, P., 1999. Interaction between faulting, drainage and sedimentation in extensional hanging-wall syncline basins: Example of the Oligocene Matelles basin (Gulf of Lion rifted margin, SE France). Geological Society, London, Special Publications 156, 81–108.

Benedicto, A., Schultz, R.A., 2010. Stylolites in limestone: Magnitude of contractional strain accommodated and scaling relationships. Journal of Structural Geology 32, 1250–1256. https://doi.org/10.1016/j.jsg.2009.04.020

Berg, S.S., Skar, T., 2005. Controls on damage zone asymmetry of a normal fault zone: outcrop analyses of a segment of the Moab fault, SE Utah. Journal of Structural Geology 27, 1803–1822. https://doi.org/10.1016/j.jsg.2005.04.012

Billi, A., Salvini, F., Storti, F., 2003. The damage zone-fault core transition in carbonate rocks: implications for fault growth, structure and permeability. Journal of Structural Geology 25, 1779–1794. https://doi.org/10.1016/S0191-8141(03)00037-3

Bisdom, K., Gauthier, B.D.M., Bertotti, G., Hardebol, N.J., 2014. Calibrating discrete fracture-network models with a carbonate three-dimensional outcrop fracture network: Implications for naturally fractured reservoir modeling. AAPG Bulletin 98, 1351–1376. https://doi.org/10.1306/02031413060

Blenkinsop, T.G., 2008. Relationships between faults, extension fractures and veins, and stress. Journal of Structural Geology 30, 622–632. https://doi.org/10.1016/j.jsg.2008.01.008

Bohnenstiehl, D.R., Carbotte, S.M., 2001. Faulting patterns near 19 30′ S on the East Pacific Rise: Fault formation and growth at a superfast spreading center. Geochemistry, Geophysics, Geosystems 2.

Caine, J.S., Evans, J.P., Forster, C.B., 1996. Fault zone architecture and permeability structure. Geology 24, 1025–1028.

Chester, F.M., Logan, J.M., 1986. Implications for mechanical properties of brittle faults from observations of the Punchbowl fault zone, California. Pure and Applied Geophysics 124, 79–106.

Childs, C., Manzocchi, T., Walsh, J.J., Bonson, C.G., Nicol, A., Schöpfer, M.P.J., 2009. A geometric model of fault zone and fault rock thickness variations. Journal of Structural Geology 31, 117–127. https://doi.org/10.1016/j.jsg.2008.08.009

Choi, J.-H., Edwards, P., Ko, K., Kim, Y.-S., 2016. Definition and classification of fault damage zones: A review and a new methodological approach. Earth-Science Reviews 152, 70–87. https://doi.org/10.1016/j.earscirev.2015.11.006

Cladouhos, T.T., Marrett, R., 1996. Are fault growth and linkage models consistent with power-law distributions of fault lengths? Journal of Structural Geology 18, 281–293.

Clark, C.D., Wilson, C., 1994. Spatial analysis of lineaments. Comput. Geosci. 20, 1237–1258. doi:10.1016/0098-3004(94)90073-6

Cowie, P.A., Sornette, D., Vanneste, C., 1995. Multifractal scaling properties of a growing fault population. Geophysical Journal International 122, 457–469.

Cowie, P.A., Shipton, Z.K., 1998. Fault tip displacement gradients and process zone dimensions. Journal of Structural Geology 20, 983–997. https://doi.org/0191-8141/98

Davatzes, N.C., Eichhubl, P., Aydin, A., 2005. Structural evolution of fault zones in sandstone by multiple deformation mechanisms: Moab fault, southeast Utah. Geological Society of America Bulletin 117, 135–148.

Dawers, N.H., Anders, M.H., Scholz, C.H., 1993. Growth of normal faults: Displacement-length scaling. Geology 21, 1107–1110.

de Joussineau, G., Aydin, A., 2007. The evolution of the damage zone with fault growth in sandstone and its multiscale characteristics. Journal of Geophysical Research 112. https://doi.org/10.1029/2006JB004711

de Joussineau, G., Mutlu, O., Aydin, A., Pollard, D.D., 2007. Characterization of strike-slip fault–splay relationships in sandstone. Journal of Structural Geology 29, 1831–1842. https://doi.org/10.1016/j.jsg.2007.08.006

Dershowitz, W.S., 1984. Rock joint systems. Massachusetts Institute of Technology.

653   Du Bernard, X., Labaume, P., Darcel, C., Davy, P., Bour, O., 2002. Cataclastic slip band
654   distribution in normal fault damage zones, Nubian sandstones, Suez rift. Journal of
655   Geophysical Research: Solid Earth 107, ETG 6-1-ETG 6-12.
656   https://doi.org/10.1029/2001JB000493
657   Evans, J.P., 1990. Thickness-displacement relationships for fault zones. Journal of Structural
658   Geology 12, 1061–1065. https://doi.org/10.1016/0191-8141(90)90101-4
659   Faulkner, D.R., Jackson, C.A.L., Lunn, R.J., Schlische, R.W., Shipton, Z.K., Wibberley,
660   C.A.J., Withjack, M.O., 2010. A review of recent developments concerning the
661   structure, mechanics and fluid flow properties of fault zones. Journal of Structural
662   Geology 32, 1557–1575. https://doi.org/10.1016/j.jsg.2010.06.009
663   Faulkner, D.R., Mitchell, T.M., Healy, D., Heap, M.J., 2006. Slip on "weak" faults by the
664   rotation of regional stress in the fracture damage zone. Nature 444, 922–925.
665   https://doi.org/10.1038/nature05353
666   Faulkner, D.R., Mitchell, T.M., Jensen, E., Cembrano, J., 2011. Scaling of fault damage zones
667   with displacement and the implications for fault growth processes. Journal of
668   Geophysical Research 116. https://doi.org/10.1029/2010JB007788
669   Flodin, E., 2003. Structural evolution, petrophysics, and large-scale permeability of faults in
670   sandstone, Valley of Fire.
671   Fossen, H., 2016. Structural geology. Cambridge University Press.
672   Fossen, H., Hesthammer, J., 2000. Possible absence of small faults in the Gullfaks Field,
673   northern North Sea: implications for downscaling of faults in some porous sandstones.
674   Journal of Structural Geology 22, 851–863.
675   Fossen, H., Rotevatn, A., 2016. Fault linkage and relay structures in extensional settings—A
676   review. Earth-Science Reviews 154, 14–28.
677   https://doi.org/10.1016/j.earscirev.2015.11.014
678   González, Á., 1989. Análisis tectosedimentario del terciario del borde SE de la depresión del
679   Ebro (sector bajoaragonés y cubetas ibéricas marginales.
680   Gratier, J.-P., Renard, F., Labaume, P., 1999. How pressure solution creep and fracturing
681   processes interact in the upper crust to make it behave in both a brittle and viscous
682   manner. Journal of Structural Geology 21, 1189–1197.
683   Griffith, W.A., Rosakis, A., Pollard, D.D., Ko, C.W., 2009. Dynamic rupture experiments
684   elucidate tensile crack development during propagating earthquake ruptures. Geology
685   37, 795–798. https://doi.org/10.1130/G30064A.1
686   Gupta, A., Scholz, C.H., 2000. A model of normal fault interaction based on observations and
687   theory. Journal of Structural Geology 22, 865–879.
688   Hadizadeh, J., Law, R.D., 1991. Water-weakening of sandstone and quartzite deformed at
689   various stress and strain rates. International Journal of Rock Mechanics and Mining
690   Sciences & Geomechanics Abstracts 28, 431–439. https://doi.org/10.1016/0148-
691   9062(91)90081-V
692   Johansen, T.E.S., Fossen, H., 2008. Internal geometry of fault damage zones in interbedded
693   siliciclastic sediments. Geological Society, London, Special Publications 299, 35–56.
694   https://doi.org/10.1144/SP299.3
695   Jourde, H., Flodin, E.A., Aydin, A., Durlofsky, L.J., Wen, X.-H., 2002. Computing
696   permeability of fault zones in eolian sandstone from outcrop measurements. AAPG
697   Bulletin 86, 1187–1200.
698   Kim, Y.-S., Peacock, D.C.P., Sanderson, D.J., 2004. Fault damage zones. Journal of
699   Structural Geology 26, 503–517. https://doi.org/10.1016/j.jsg.2003.08.002
700   Knott, S.D., Beach, A., Brockbank, P.J., Brown, J.L., McCallum, J.E., Welbon, A.I., 1996.
701   Spatial and mechanical controls on normal fault populations. Journal of Structural
702   Geology 18, 359–372.

Manighetti, I., King, G.C.P., Gaudemer, Y., Scholz, C.H., Doubre, C., 2001. Slip accumulation and lateral propagation of active normal faults in Afar. Journal of Geophysical Research: Solid Earth 106, 13667–13696.

Manighetti, I., King, G., Sammis, C.G., 2004. The role of off-fault damage in the evolution of normal faults. Earth and Planetary Science Letters 217, 399–408. https://doi.org/10.1016/S0012-821X(03)00601-0

Mansfield, C.S., Cartwright, J.A., 1996. High resolution fault displacement mapping from three-dimensional seismic data: evidence for dip linkage during fault growth. Journal of Structural Geology 18, 249–263. https://doi.org/10.1016/S0191-8141(96)80048-4

Maqbool, A.-R., Moustafa, A.R., Dowidar, H., Yousef, M., 2016. Architecture of fault damage zones of normal faults, Gebel Ataqa area, Gulf of Suez rift, Egypt. Marine and Petroleum Geology 77, 43–53. https://doi.org/10.1016/j.marpetgeo.2016.04.012

Marchal, D., Guiraud, M., Rives, T., Van Den Driessche, J., 1998. Space and time propagation processes of normal faults. Geological Society, London, Special Publications 147, 51–70.

Martín-Martín, J.D., Gomez-Rivas, E., Bover-Arnal, T., Travé, A., Salas, R., Moreno-Bedmar, J.A., Tomás, S., Corbella, M., Teixell, A., Vergés, J., Stafford, S.L., 2013. The Upper Aptian to Lower Albian syn-rift carbonate succession of the southern Maestrat Basin (Spain): Facies architecture and fault-controlled stratabound dolostones. Cretaceous Research 41, 217–236. https://doi.org/10.1016/j.cretres.2012.12.008

McGrath, A.G., Davison, I., 1995. Damage zone geometry around fault tips. Journal of Structural Geology 17, 1011–1024.

Micarelli, L., Benedicto, A., Wibberley, C.A.J., 2006. Structural evolution and permeability of normal fault zones in highly porous carbonate rocks. Journal of Structural Geology 28, 1214–1227. https://doi.org/10.1016/j.jsg.2006.03.036

Micarelli, L., Moretti, I., Daniel, J.M., 2003. Structural properties of rift-related normal faults: the case study of the Gulf of Corinth, Greece. Journal of Geodynamics 36, 275–303. https://doi.org/10.1016/S0264-3707(03)00051-6

Mitchell, T.M., Faulkner, D.R., 2012. Towards quantifying the matrix permeability of fault damage zones in low porosity rocks. Earth and Planetary Science Letters 339–340, 24–31. https://doi.org/10.1016/j.epsl.2012.05.014

Mitchell, T.M., Faulkner, D.R., 2009. The nature and origin of off-fault damage surrounding strike-slip fault zones with a wide range of displacements: A field study from the Atacama fault system, northern Chile. Journal of Structural Geology 31, 802–816. https://doi.org/10.1016/j.jsg.2009.05.002

Nebot Miralles, M., Guimerà i Rosso, J.J., 2016. Structure of an inverted basin from subsurface and field data. Geologica Acta 14, 0155–177.

Nicol, A., Watterson, J., Walsh, J.J., Childs, C., 1996. The shapes, major axis orientations and displacement patterns of fault surfaces. Journal of Structural Geology 18, 235–248.

Novakova, L., Pavlis, T.L., 2017. Assessment of the precision of smart phones and tablets for measurement of planar orientations: A case study. Journal of Structural Geology 97, 93–103. https://doi.org/10.1016/j.jsg.2017.02.015

Peacock, D.C.P., 2001. The temporal relationship between joints and faults. Journal of Structural Geology 23, 329–341.

Peacock, D.C.P., 2003. Scaling of transfer zones in the British Isles. Journal of Structural Geology 25, 1561–1567.

Peacock, D.C.P., Sanderson, D.J., 1991. Displacements, segment linkage and relay ramps in normal fault zones. Journal of Structural Geology 13, 721–733.

Peacock, D.C.P., Dimmen, V., Rotevatn, A., Sanderson, D.J., 2017. A broader classification of damage zones. Journal of Structural Geology 102, 179–192. https://doi.org/10.1016/j.jsg.2017.08.004

Perrin, C., Manighetti, I., Gaudemer, Y., 2016. Off-fault tip splay networks: A genetic and generic property of faults indicative of their long-term propagation. Comptes Rendus Geoscience 348, 52–60. https://doi.org/10.1016/j.crte.2015.05.002

Petit, J.-P., Mattauer, M., 1995. Palaeostress superimposition deduced from mesoscale structures in limestone: the Matelles exposure, Languedoc, France. Journal of Structural Geology 17, 245249–247256.

Petit, J.-P., Wibberley, C.A., Ruiz, G., 1999. Crack–seal', slip: a new fault valve mechanism? Journal of Structural Geology 21, 1199–1207.

Philit, S., Soliva, R., Castilla, R., Ballas, G., Taillefer, A., 2018. Clusters of cataclastic deformation bands in porous sandstones. Journal of Structural Geology 114, 235–250. https://doi.org/10.1016/j.jsg.2018.04.013

Robert, F., Boullier, A.-M., Firdaous, K., 1995. Gold-quartz veins in metamorphic terranes and their bearing on the role of fluids in faulting. Journal of Geophysical Research: Solid Earth 100, 12861–12879. https://doi.org/10.1029/95JB00190

Roca, E., Guimerà, J., 1992. The Neogene structure of the eastern Iberian margin: Structural constraints on the crustal evolution of the Valencia trough (western Mediterranean). Tectonophysics 203, 203–218. https://doi.org/10.1016/0040-1951(92)90224-T

Roche, V., Homberg, C., Rocher, M., 2012. Architecture and growth of normal fault zones in multilayer systems: A 3D field analysis in the South-Eastern Basin, France. Journal of Structural Geology 37, 19–35. https://doi.org/10.1016/j.jsg.2012.02.005

Salas, R., Casas, A., 1993. Mesozoic extensional tectonics, stratigraphy and crustal evolution during the Alpine cycle of the eastern Iberian basin. Tectonophysics 228, 33–55.

Salas, R., García-Senz, J., Guimerà, J., Bover-Arnal, T., 2011. Opening of the Atlantic and development of the Iberian intraplate rift basins during the late Jurassic-early Cretaceous. CM 2010-Abstracts 3, 245–248.

Salas, R., Guimerà, J., Mas, R., Martín-Closas, C., Meléndez, A., Alonso, A., 2001. Evolution of the Mesozoic central Iberian Rift System and its Cainozoic inversion (Iberian chain). Peri-Tethys Memoir 6, 145–185.

Savage, J.C., Burford, R.O., 1973. Geodetic determination of relative plate motion in central California. Journal of Geophysical Research 78, 832–845.

Savage, H.M., Brodsky, E.E., 2011. Collateral damage: Evolution with displacement of fracture distribution and secondary fault strands in fault damage zones. Journal of Geophysical Research 116, 1–14. https://doi.org/10.1029/2010JB007665

Schlische, R.W., Young, S.S., Ackermann, R.V., Gupta, A., 1996. Geometry and scaling relations of a population of very small rift-related normal faults. Geology 24, 683–686.

Scholz, C.H., Cowie, P.A., 1990. Determination of total strain from faulting using slip measurements. Nature 346, 837.

Schueller, S., Braathen, A., Fossen, H., Tveranger, J., 2013. Spatial distribution of deformation bands in damage zones of extensional faults in porous sandstones: Statistical analysis of field data. Journal of Structural Geology 52, 148–162. https://doi.org/10.1016/j.jsg.2013.03.013

Séranne, M., Benedicto, A., Labaum, P., Truffert, C., Pascal, G., 1995. Structural style and evolution of the Gulf of Lion Oligo-Miocene rifting: Role of the Pyrenean orogeny. Marine and Petroleum Geology 12, 809–820.

Shipton, Z.K., Cowie, P.A., 2003. A conceptual model for the origin of fault damage zone structures in high-porosity sandstone. Journal of Structural Geology 25, 333–344.

801 Shipton, Z.K., Cowie, P.A., 2001. Damage zone and slip-surface evolution over µm to km
802   scales in high-porosity Navajo sandstone, Utah. Journal of Structural Geology 23,
803   1825–1844.
804 Sibson, R.H., 2000. Fluid involvement in normal faulting. Journal of Geodynamics 29, 469–
805   499.
806 Soliva, R., Benedicto, A., 2004. A linkage criterion for segmented normal faults. Journal of
807   Structural Geology 26, 2251–2267. https://doi.org/10.1016/j.jsg.2004.06.008
808 Soliva, R., Benedicto, A., Maerten, L., 2006. Spacing and linkage of confined normal faults:
809   Importance of mechanical thickness. Journal of Geophysical Research 111.
810   https://doi.org/10.1029/2004JB003507
811 Soliva, R., and R. A. Schultz, 2008. Distributed and localized faulting in extensional settings :
812   Insight from the North Ethiopian RiftAfar transition area, Tectonics, 27, TC2003,
813   doi:10.1029/2007TC002148.
814 Soliva, R., Maerten, F., Petit, J.-P., Auzias, V., 2010. Field evidences for the role of static
815   friction on fracture orientation in extensional relays along strike-slip faults:
816   Comparison with photoelasticity and 3-D numerical modeling. Journal of Structural
817   Geology 32, 1721–1731. https://doi.org/10.1016/j.jsg.2010.01.008
818 Steer, P., Bigot, A., Cattin, R., Soliva, R., 2011. In-situ characterization of the effective
819   elasticity of a fault zone, and its relationship to fracture spacing. Journal of Structural
820   Geology 33, 1541–1553. https://doi.org/10.1016/j.jsg.2011.09.009
821 Taha, M., 1986. Apport de la microtectonique cassante aux problemes des trajectoires de
822   contraintes et de leurs perturbations (exemple du Nord de Montpellier).
823 Taillefer, A., Soliva, R., Guillou-Frottier, L., Le Goff, E., Martin, G., Seranne, M., 2017.
824   Fault-Related Controls on Upward Hydrothermal Flow: An Integrated Geological
825   Study of the Têt Fault System, Eastern Pyrénées (France). Geofluids 2017, 1–19.
826   https://doi.org/10.1155/2017/8190109
827 Torabi, A., Berg, S.S., 2011. Scaling of fault attributes: A review. Marine and Petroleum
828   Geology 28, 1444–1460. https://doi.org/10.1016/j.marpetgeo.2011.04.003
829 Toussaint, R., Aharonov, E., Koehn, D., Gratier, J.-P., Ebner, M., Baud, P., Rolland, A.,
830   Renard, F., 2018. Stylolites: A review. Journal of Structural Geology 114, 163–195.
831   https://doi.org/10.1016/j.jsg.2018.05.003
832 Wibberley, C.A.J., Yielding, G., Di Toro, G., 2008. Recent advances in the understanding of
833   fault zone internal structure: a review. Geological Society, London, Special
834   Publications 299, 5–33. https://doi.org/10.1144/SP299.2
835 Wilson, J.., Chester, J.., Chester, F.., 2003. Microfracture analysis of fault growth and wear
836   processes, Punchbowl Fault, San Andreas system, California. Journal of Structural
837   Geology 25, 1855–1873. https://doi.org/10.1016/S0191-8141(03)00036-1
838

Figures Captions

840

841   **Fig. 1** Locations and geological schemes of the studied areas. a) Cenozoic cover map in

842   Languedoc area. Red box 1 is the St Clement fault study area. Red box 2 is the Taurac fault

843   study area. The regional stratigraphic column shows, in red, layers where damage

844   measurements are made in this study. Stereogram shows the average fracture and fault

845   orientations in these areas. Cross section according to the profile A-A'. b) Cenozoic cover

846   map in Maestrat study area. Red box 3 is the Sant Mateu study area and red box 4 is the

847   Aliaga study area. Similarly to a), the regional stratigraphic column, stereogram and cross

848   section according to profile B-B' are also represented for this area.

849

850

851   **Fig. 2** Brittle structures in carbonate rocks measured in the field. a) Joint sealed by sparite

852   mineralization. b) Tension crack Mode I opening sealed by sparite mineralization. c)

853   Horizontal stylolite associated with vertical fracture. d) Normal fault with 1.5 m displacement.

854   This fault has been selected for scanline measurement (Fig. 5a).

855

856

857   **Fig. 3** Scheme for the damage zone thickness correction using the angle between the

858   scanline and the normal to the fault plane.

859

860

861   **Fig. 4** Geological and mapping data in Sant mateu area. a) Sant Mateu master fault trace.

862   b) Geological map of the Sant Mateu area. Stereograms correspond to field fracture

863   measurements on one outcrop. c) Average orientation of the 1358 lineaments traces on map.

864   d) Colour chart for stereogram.

865

866

867   **Fig. 5** Total scanlines sampled in the four study areas. a), c), d) have been sampled in St

868   Clement, b) Taurac fault, e), f), g), h), i) at Sant Mateu and j), k), l) in Aliaga area. Yellow

869   dashed line marked the DZ boundary estimated with cumulative frequency curve. Faults with

870   0.5 m and 1 m displacement have only one inflection due to the small DZ thickness. Grey

871   boxes represent all the gaps where the outcrop quality prevents measurement.

872

873

874   **Fig. 6** Detail S8 scanline and average fractures orientations on normal fault in Sant Mateu.

875   a) Picture of the fault and the outcrop where the scanline was done (blue line). d) Scanline

876   histogram with fracture frequency as a function of the distance to the fault. The DZ thickness

877   (yellow dashed line) is determined by the inflection of the cumulative frequency curve (grey

878   dot). c) (up) Rose diagram of the fracture orientations classified in function of their types. The

879   length of each segment represents the proportional orientation for each fracture types. (down)

880   Rose diagram of unclassified fracture orientations, proportions of orientations are represented

881   independently to the fracture types.

882

883

884   **Fig. 7** Damage zone thickness data for this study as a function of displacement. Data show

885   an accurate linear law mainly define by normal faults, in carbonate rocks. a) log-log diagram

886   for all 12 scanlines, b) Same as a) with linear axis. The two faults with displacements over

887   100 m show significant deviation of the linear correlation. c) and d) Same as a) and b) without

888   outliers (S2 and S4).

889

890

891   **Fig. 8** Total fault zone thickness as a function of displacement modified from Savage and

892   Brodsky, 2011. Linear scaling is well defined for faults displacement between 1 m and 100 m

893   in carbonate rocks. Two faults over 100 m displacement seem to start the bending of the

894   scaling law trend. Têt fault is a normal fault in Eastern Pyrénées, affecting granit and

895   mylonite. Point with dot contour represent fault DZ evaluated in map view with secondary

896   fault damage, for St Clement fault, Sant Mateu master faults and Têt fault (from Taillefer et

897   al., 2017).

898

899

900   **Fig. 9** Model of fault segmentation and damage zone growth. a) 3D model of segmented

901   master fault with secondary faults and associated Mode I fracture damage zone. b) Spacing

902   (S) between linking master faults as function of the displacement. c) Mode I damage zone

903   increasing as function of the displacement and segment linkage show in d). d) Model of Mode

904   I fracturing damage increased by fault segment linkage and tip secondary fault incorporation.

905

906

907   **Fig. 10** a) Diagram for Mode I and secondary fault damage zone. b) Mode I damage zone

908   growth by fault segments interaction. c) Fault segment linkage model inhibited by brittle

909   ductile transition.

910

911   **Appendices**

912

913   **Fig. A1** Geological and mapping data in St Clement area. a) Geological map of the St

914   Clement area. Stereograms correspond to field fracture measurements on one outcrop. b)

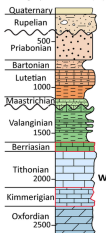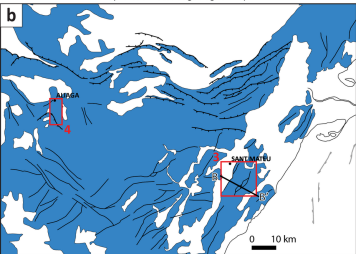915   Colour chart for stereogram. c) Average orientation of the 532 lineaments traces on map.

916

917

918

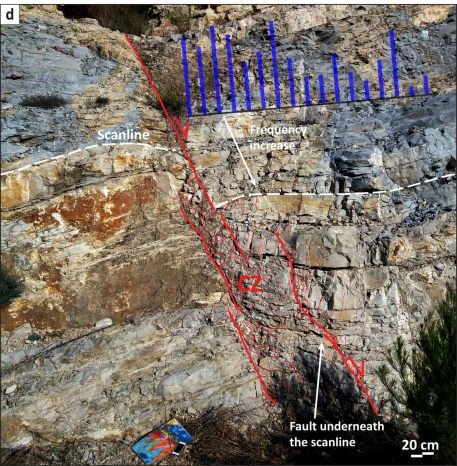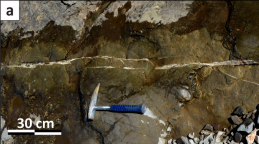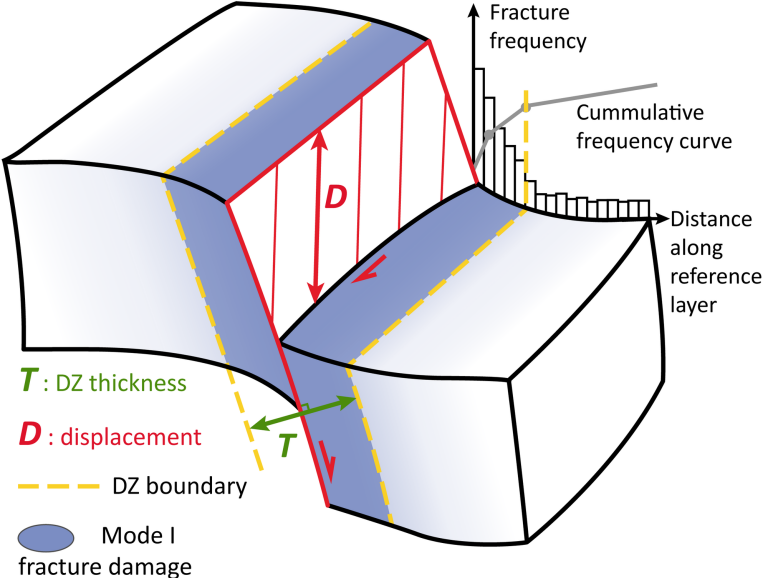**a** Synthetic Languedoc geological map

Stratigraphic column (m)

Quaternary
Rupelian
Priabonian
Bartonian
Lutetian
Maastrichtian
Valanginian
Berriasian
Tithonian
Kimmerigian
Oxfordian

Cevennes Fault

Nîmes Fault

MONTPELLIER

0   10 km

France

N
W   Faults   E
Fractures
S

A   The Matelles fault   St Clement fault   Prades fault   A'

Oligocene   Priabonian Middle Eocene   Lez fault   Lower Eocene   Teyran fault

Valanginian
Berriasian
Jurassic

Trias

Paleozoic

Cenozoic cover

Mesozoic cover

Basement

Faults

b Synthetic Maestrat geological map

Stratigraphic column (m)

Quaternary
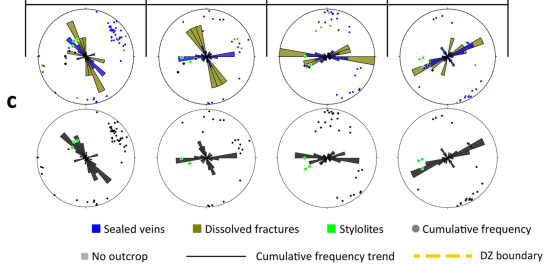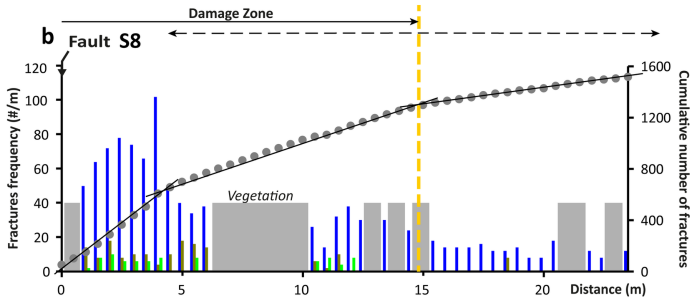Miocene
Albian
Aptien
Barremian
Hauterivian
Berriasian
Tithonian
Kimmerigian
Oxfordian

ALPGA

SANT MATEU

0   10 km

Spain

N
W   E
S

B   Salsadella fault   Miocene   S. Magdalena fault   B'

Berriasian   Oxfordian   Kimmeridgian   Tithonian

0 km
500
1000

a

30 cm

b

5 cm

c

Stylolite

2 cm

d

Scanline

Frequency increase

CZ

Fault underneath the scanline

20 cm

Fracture frequency

Cummulative frequency curve

Distance along reference layer

T : DZ thickness

D : displacement

DZ boundary

Mode I fracture damage

a Fig. part b

Tip secondary fault damage

Basin infill

2 km

N

b

Master fault

Secondary fault

Minor secondary fault

Lithologies

Quaternary undifferentiated

Quaternary breccia

Hauterivian-Barremian

Berriasian-Valanginian

Upper Jurassic

N

0 1 2 km

La Salzadella

c

10 15 20

N = 1358

d

Fracture pole

Fractures

Fault plane pole

Fault

Stylolite pole

a E   20 m   W

Scanline

b Fault S8

Damage Zone

Vegetation

Fractures frequency (#/m)

Cumulative number of fractures

Distance (m)

c

Sealed veins   Dissolved fractures   Stylolites   Cumulative frequency
No outcrop   Cumulative frequency trend   DZ boundary

Figure panels (a), (b), (c), (d) showing Damage Zone Thickness (m) versus Fault Displacement (m).

Panel a:
$y = 1.6x^{0.82}$
$R^2 = 0.93$

Labels: S3, S1, S7, S8, S10, S12, S9, S6, S11, S5, S2, S4

Legend: Normal, Reverse, Strike slip

Panel b:
Labels: S2, S11, S4

Legend: Normal, Reverse, Strike slip

Panel c:
$y = 1.20x^{0.95}$
$R^2 = 0.97$

Legend: Normal, Reverse, Strike slip

Panel d:
$y = 1.20x^{0.95}$
$R^2 = 0.97$

Legend: Normal, Reverse, Strike slip

a

2

1

4

DZ

3

b

D

Linked

Not linked

S

c

Accumulation of
Mode I damage by
segment linkage

D

4

3

2

1

DZ

d

1

2

3

4

Tip secondary
fault DZ

Mode I fracture damage

Spacing between linking master faults

Master fault considered in figure part c

Mode I damage thickness

Master fault not considered in figure part c

Minor secondary faults

a DZ vs D plot with points 1 and 2, and "Tip secondary fault DZ fig. part d)" annotation

b Stage 1 — DZ₁, D_1, DZ growth by segment interaction

c Stage 2 — DZ₂, D_2, Weakening by fault segment linkage, No more possible fault segments, Ductile shear

d Master fault tip at stage 2 — Mode I DZ₂, Tip secondary fault DZ, Mode I DZ₂

$DZ_1 \sim DZ_2$

$D_1 \ll D_2$

Mode I fracture damage

Master faults